



Synchrotron-based investigation of transition-metal getterability in n-type multicrystalline silicon

Ashley E. Morishige, Mallory A. Jensen, Jasmin Hofstetter, Patricia X. T. Yen, Chenlei Wang, Barry Lai, David P. Fenning, and Tonio Buonassisi

Citation: *Applied Physics Letters* **108**, 202104 (2016); doi: 10.1063/1.4950765

View online: <http://dx.doi.org/10.1063/1.4950765>

View Table of Contents: <http://scitation.aip.org/content/aip/journal/apl/108/20?ver=pdfcov>

Published by the [AIP Publishing](#)

Articles you may be interested in

[Exceptional gettering response of epitaxially grown kerfless silicon](#)

J. Appl. Phys. **119**, 065101 (2016); 10.1063/1.4940947

[Synchrotron-based analysis of chromium distributions in multicrystalline silicon for solar cells](#)

Appl. Phys. Lett. **106**, 202104 (2015); 10.1063/1.4921619

[Competitive gettering of iron in silicon photovoltaics: Oxide precipitates versus phosphorus diffusion](#)

J. Appl. Phys. **116**, 053514 (2014); 10.1063/1.4892015

[Dependence of phosphorus gettering and hydrogen passivation efficacy on grain boundary type in multicrystalline silicon](#)

J. Appl. Phys. **114**, 244902 (2013); 10.1063/1.4856215

[Effect of oxygen ambient during phosphorous diffusion on silicon solar cell](#)

J. Renewable Sustainable Energy **4**, 033105 (2012); 10.1063/1.4717513

The image shows the cover of an Applied Physics Reviews journal issue. It features a blue and orange color scheme with a molecular structure background. The text 'NEW Special Topic Sections' is prominently displayed in white. Below it, 'NOW ONLINE' is written in yellow, followed by the title 'Lithium Niobate Properties and Applications: Reviews of Emerging Trends' in white. The AIP Applied Physics Reviews logo is in the bottom right corner.

NEW Special Topic Sections

NOW ONLINE
Lithium Niobate Properties and Applications:
Reviews of Emerging Trends

AIP Applied Physics
Reviews

Synchrotron-based investigation of transition-metal getterability in *n*-type multicrystalline silicon

Ashley E. Morishige,^{1,a)} Mallory A. Jensen,¹ Jasmin Hofstetter,¹ Patricia X. T. Yen,¹ Chenlei Wang,² Barry Lai,³ David P. Fenning,^{1,4} and Tonio Buonassisi^{1,b)}

¹Massachusetts Institute of Technology, Cambridge, Massachusetts 02139, USA

²Supreme Inc., Sunnyvale, California 94085, USA

³Advanced Photon Source, Argonne National Laboratory, Argonne, Illinois 60439, USA

⁴University of California, San Diego, La Jolla, California 92093, USA

(Received 21 March 2016; accepted 1 May 2016; published online 17 May 2016)

Solar cells based on *n*-type multicrystalline silicon (mc-Si) wafers are a promising path to reduce the cost per kWh of photovoltaics; however, the full potential of the material and how to optimally process it are still unknown. Process optimization requires knowledge of the response of the metal-silicide precipitate distribution to processing, which has yet to be directly measured and quantified. To supply this missing piece, we use synchrotron-based micro-X-ray fluorescence (μ -XRF) to quantitatively map >250 metal-rich particles in *n*-type mc-Si wafers before and after phosphorus diffusion gettering (PDG). We find that 820 °C PDG is sufficient to remove precipitates of fast-diffusing impurities and that 920 °C PDG can eliminate precipitated Fe to below the detection limit of μ -XRF. Thus, the evolution of precipitated metal impurities during PDG is observed to be similar for *n*- and *p*-type mc-Si, an observation consistent with calculations of the driving forces for precipitate dissolution and segregation gettering. Measurements show that minority-carrier lifetime increases with increasing precipitate dissolution from 820 °C to 880 °C PDG, and that the lifetime after PDG at 920 °C is between the lifetimes achieved after 820 °C and 880 °C PDG. *Published by AIP Publishing.*

[<http://dx.doi.org/10.1063/1.4950765>]

For photovoltaics (PV), *n*-type multicrystalline silicon (mc-Si) wafers are an attractive alternative to *p*-type mc-Si wafers. One advantage is that some common metal point defects, notably interstitial iron, are less recombination active in *n*-type than in *p*-type Si.^{1–3} It has been shown that phosphorus diffusion gettering (PDG) can increase the lifetime of *n*-type mc-Si, including in low-lifetime ingot border regions,^{4–7} and that industrially relevant efficiencies are achievable.⁸ For *p*-type mc-Si, simulation of the redistribution of metal impurities during PDG and the resulting lifetime impact has enabled development of PDG processes that improve yield and extract higher performance, especially in border regions and the top of the ingot.^{9–12} For *n*-type mc-Si, lifetime models for point defects¹ and iron-silicide precipitates¹³ have been developed. The precipitated metal distribution for a range of PDG temperatures has yet to be measured and quantified, hampering the development of modeling and processing that is co-optimized for manufacturing throughput and high performance. In this contribution, we mapped the precipitated metal distributions in *n*-type mc-Si wafers before and after several processes. We also report spatially resolved lifetime improvement associated with each process.

Three nearly vertically adjacent wafers with thickness $205 \pm 5 \mu\text{m}$ and resistivity of $2 \Omega\text{cm}$ were selected from the middle height of a corner brick of a 6N's purity compensated *n*-type upgraded metallurgical grade (UMG) industrially produced Generation 5 cast mc-Si ingot. The low-lifetime “red zone” region formed near the crucible walls during casting was identified with microwave photoconductance decay

using a *Semilab WT-2000*. All samples were CP4 etched to a thickness of $190 \mu\text{m}$ to remove saw damage.

From each wafer, several samples were selected for characterization and processing. To quantify the total concentrations of metal impurities in the as-grown wafers, 1 g samples from the red zone were selected from two of the wafers for inductively coupled plasma mass spectroscopy (ICP-MS). To map the precipitated impurity distribution before and after PDG, a $1 \times 1 \text{cm}^2$ sample was selected from the red zone of each wafer for synchrotron-based micro-X-ray fluorescence spectroscopy (μ -XRF) measurements. For photoconductance-calibrated photoluminescence imaging (PC-PL), $4 \times 5 \text{cm}^2$ lifetime samples adjacent to each μ -XRF sample were cut.

The μ -XRF and electrical characterization samples were phosphorus-diffused in a Tystar Titan 3800 tube furnace at 820, 880, and 920 °C for 60 min followed by a slow cool at $\sim 4 \text{°C/min}$ to 600 °C, at which point they were unloaded from the furnace. The time–temperature profiles and their respective sheet resistances measured on a *p*-type Cz-Si control sample processed at the same time are shown in Figure S1.¹⁴ The same region on each sample was measured before and after PDG. To test the effect of the time spent at diffusion temperature on the precipitated metal distribution, μ -XRF was also measured on a sample that was diffused at 820 °C for only 30 min followed by the same slow cool (S820 °C).

μ -XRF was measured at Argonne National Laboratory's Advanced Photon Source Beamline 2-ID-D using an incident X-ray energy of 10 keV with data mapped in step-by-step scanning mode. A $\Sigma 33$ grain boundary that is present in all three μ -XRF samples was identified with electron backscatter diffraction (EBSD). For the post-PDG μ -XRF measurements, to compare precipitates near the surface that were

^{a)}E-mail: aemorish@alum.mit.edu

^{b)}E-mail: buonassisi@mit.edu

observed in the as-grown μ -XRF measurements, the phosphorus-diffused layer was left intact. μ -XRF maps were measured along the grain boundary in 220 nm steps with a spot size of 209 nm at full-width half-maximum. To be considered a detected precipitate, a given pixel had to have a metal loading above both of the following noise floors. The statistical detection limit (SDL) was set at four standard deviations above the mean of the noise.¹⁵ The theoretical minimum detection limit (MDL) was calculated from the measurements of NIST standards 1832 and 1833 measured in the same experimental configuration as the respective sample. We assume that the detected Fe in these mc-Si wafers is in β -FeSi₂ precipitates¹⁶ in which $3.76 \times 10^{-23} \text{ cm}^3$ is the effective volume of one Fe atom.¹⁷ We further assume that precipitates are spherical and that for size calculations they are at the sample surface as in Refs. 10, 15, 18, and 19. Further details are available in Refs. 10 and 18.

The PC-PL images were captured using the same experimental setup as in Jensen *et al.*¹⁵ and originally described in Herlufsen *et al.*²⁰ Surface passivation is the same as in Jensen *et al.*¹⁵ To enable measurement of the bulk lifetime, before the post-PDG surface passivation, 10 μm of the samples were etched with CP4, removing the phosphosilicate glass and the phosphorus-diffused layer.

The ICP-MS results (Figure S2) reveal V, Fe, Ni, Co, Cu, Zn, Zr, Nb, Ag, and W in the red zone.¹⁴ The concentration of Fe is $4.7 \times 10^{14} \text{ cm}^{-3}$ while Ni, Co, and Cu are at concentrations of $2.4 \times 10^{13} \text{ cm}^{-3}$, $1.6 \times 10^{13} \text{ cm}^{-3}$, and $1.6 \times 10^{13} \text{ cm}^{-3}$, respectively. Consistent with the high concentrations identified by ICP-MS, the as-grown μ -XRF measurements revealed Fe-, Co-, Ni-, and Cu-containing particles co-located along the Σ 33 grain boundary (Figure S3).¹⁴ Zr, Nb, Mo, Ag, Sn, W, and Au are not detected in the as-grown μ -XRF measurements because their $K\alpha$ binding energies are greater than the 10 keV incident energy.²¹ We hypothesize that any Zn particles are too small to detect because Zn diffuses relatively slowly in silicon and thus may be found in a high spatial density of small precipitates.²² V, Cr, and Mn were also not detected in quantities above the noise floor of the μ -XRF measurements. ICP-MS was measured on two red zone and two bulk samples from the same wafers. The full results are shown in Figure S4.¹⁴

After all of the PDG processes studied, Fe is the only metal that persists at detectable levels in the μ -XRF measurements. Shown in Figure 1 is the Fe channel of quantified μ -XRF maps of a $\sim 50 \mu\text{m}$ -wide portion of the grain boundary before and after each 60 min PDG process. Bright yellow pixels have high Fe loading, likely along the plane of the grain boundary. PDG at 820 °C reduced the number of Fe precipitates from 39 to 28, a 28% removal. PDG at 880 °C reduced the number of precipitate from 58 to 36, a 38% removal. Finally, PDG at 920 °C removed all 60 Fe precipitates, to within the detection limit, a 100% removal. The post-PDG μ -XRF maps for the S820 °C and 820 °C processes are shown in Figure S5.¹⁴

The Fe maps of Figure 1 were further analyzed to quantify the precipitate size distribution before and after PDG. Figure S6 shows the number of Fe atoms per precipitate and the corresponding calculated precipitate radius before and after each process.¹⁴ As-grown, Fe-rich precipitates ranging in size from 8 to 30 nm were identified. After PDG at 820 °C, the mean precipitate size is similar, and the median precipitate size increases compared to the as-grown state. After PDG at 880 °C, the mean and median precipitate size decrease noticeably from the as-grown state. After the 920 °C PDG, even though the noise floor of the μ -XRF measurement after PDG was lower than that of the as-grown measurement, no precipitates were detected. To directly compare the effect of PDG at 820 and 880 °C, histograms of the precipitate size distributions are plotted in Figures 2(a) and 2(b). After PDG at 820 °C, the relative frequency of many of the precipitate sizes decreases. In contrast, PDG at 880 °C shifts the precipitate size distribution to smaller precipitates. A histogram of the precipitate sizes after PDG for the S820 °C and 820 °C process shows very similar distributions (Figure S7).¹⁴

To quantify the effect on an individual precipitate basis, for Fe precipitates identifiable before and after PDG in the maps of Figure 1, the percent reduction in the number of Fe atoms per precipitate was calculated for each precipitate, and the resulting frequency distribution of the size reduction for each process is shown in Figure 2. For PDG at 820 °C, the peak of the size reduction distribution is 45% reduction. For PDG at 880 °C, the peak of the size reduction distribution is higher at 65% reduction.

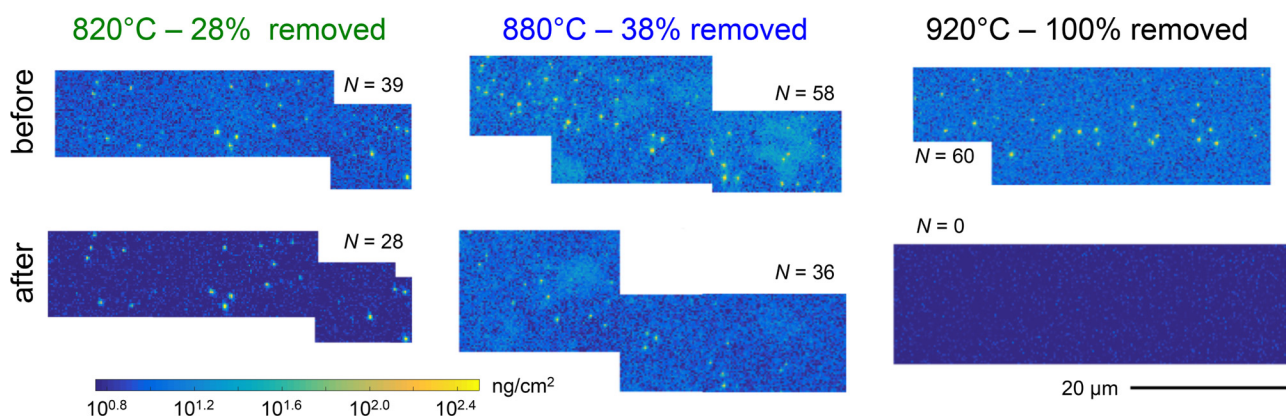


FIG. 1. μ -XRF maps of the Fe channel for $\sim 50 \mu\text{m}$ of a Σ 33 grain boundary in three nearly vertically adjacent *n*-type mc-Si samples before (*top row*) and after (*bottom row*) PDG at 820 °C (*left*), 880 °C (*center*), and 920 °C (*right*). Bright yellow pixels have high Fe loading, measured in ng/cm^2 . The number of Fe precipitates identified, N , in each map is indicated. As the PDG temperature increases, Fe precipitates are more readily dissolved. 920 °C PDG reduced Fe to undetectable levels.

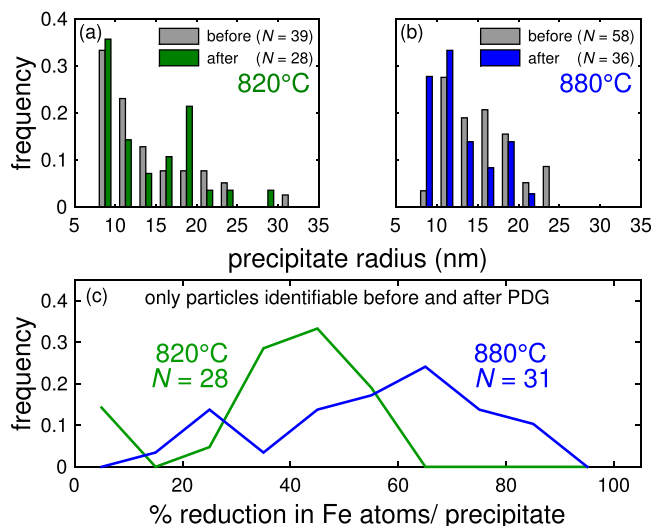


FIG. 2. Fe precipitate size distributions for precipitates in the maps of Figure 1 before and after PDG at 820 °C (a) and 880 °C (b). (c) Histogram of reduction in size of the individual precipitates for Fe-rich particles identifiable before and after PDG. PDG at 820 °C has a peak reduction of 45%. PDG at 880 °C has a peak reduction of 65%. N is the number of Fe particles included in each analysis.

The total sample area scanned after PDG was larger than that included the areas scanned before processing to ensure that all regions measured as-grown would be measured after PDG. The trends in precipitate size in the subset of the data shown in Figs. 1 and 2 are the same as those of the full data set. The full Fe μ -XRF maps are shown in Figure S8.¹⁴ The quantified Fe precipitate sizes for all of the regions mapped (shown in Figure S5 and S8) are shown in Figure S9.¹⁴

To quantify the improvement in lifetime after each process, the spatially resolved ratio of post- to pre-PDG PC-PL lifetime was calculated. Then, for each pixel, the lifetime improvement ratio was plotted as a function of the as-grown lifetime (Figure 3). PC-PL lifetime images at an average injection level of $1.4 \times 10^{14} \text{ cm}^{-3}$ before and after PDG and their ratio are shown in Figure S10.¹⁴ As-grown samples had similar lifetimes with a harmonic mean of 23 μs . After processing, the lifetimes increase for all processes by over an order of magnitude. The post-PDG harmonic mean lifetimes were 500, 575, and 520 μs for PDG at 820, 880, and 920 °C, respectively.

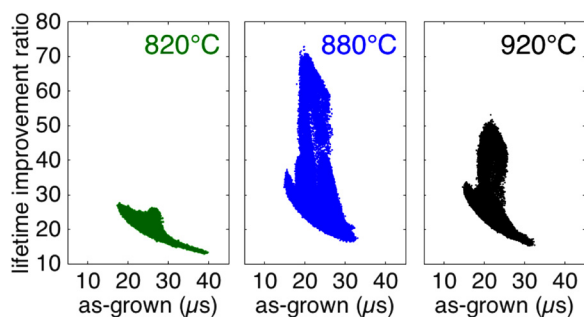


FIG. 3. Plots of the lifetime improvement ratio (PDG/ as-grown lifetime) as a function of the as-grown lifetime for each process. All processes increase lifetime. PDG at 880 °C is the most effective, followed by PDG at 920 °C. PDG at 820 °C is the least effective. Each data point is a pixel from the images shown in Figure S10.¹⁴

Our results support the hypothesis that the redistribution of metals during PDG is similar in p -type and n -type mc-Si. μ -XRF measurements of as-grown p -type mc-Si wafers with a very similar total Fe concentration of $4.4 \times 10^{14} \text{ cm}^{-3}$ revealed a similar precipitate size distribution of up to 30 nm radius particles.¹⁸ After PDG at 870 °C, precipitates of fast-diffusing species, specifically Cu, were readily removed from p -type mc-Si, but Fe precipitates persisted at a reduced level.¹⁰ For p -type mc-Si with a total Fe concentration of $\sim 10^{15} \text{ cm}^{-3}$, the median reduction in precipitate size of Fe-rich precipitates identifiable both before and after PDG increased as the PDG temperature increased.¹⁰ The median reduction after 820 °C, 870 °C, and 920 °C PDG was 84.1%, 85.3%, and 91.5%, respectively.¹⁰ For the highest temperature 920 °C PDG, we hypothesize that the Fe precipitates were reduced to below the detection limit in the n -type material because the total Fe concentration of $4.7 \times 10^{14} \text{ cm}^{-3}$ is slightly higher than the solid solubility of Fe at 920 °C,²³ making it likely that in the bulk, full dissolution was achieved at guttering temperature. The reported percent reductions in precipitate size after the 820 °C and 880 °C PDG were higher than those observed in this study. We attribute this difference to the differences in the initial Fe distribution, time-temperature profiles, and differing noise limits of the measurements. Thus, the temperature-dependence of metal redistribution in p - and n -type mc-Si studied herein is similar and, for simulation purposes, can be assumed to be the same.

We observe similar precipitate-dissolution behavior during PDG in both n - and p -type silicon, suggesting similar governing physics. Our calculations indicate that at PDG temperatures, the Fermi energy is close to or at midgap for both n - and p -type silicon. Figure 4 shows the evolution of the energy band diagram of crystalline silicon as a function of temperature for phosphorus-doped and boron-doped silicon for three different resistivity levels relevant to PV. At temperatures relevant for PDG, $>500 \text{ °C}$, in both p - and n -type Si, the intrinsic carrier concentration is high enough that the Fermi levels of the doped material approach the

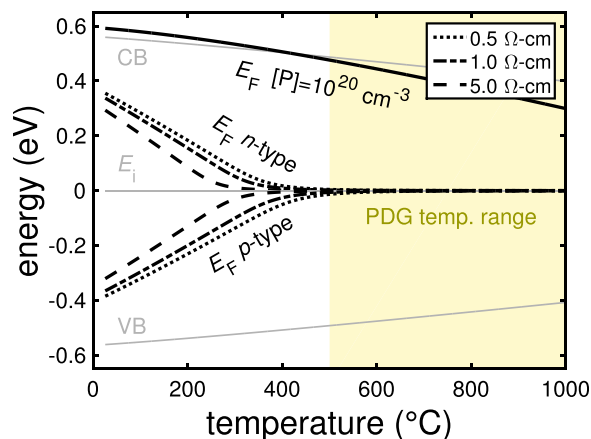


FIG. 4. Energy band diagram of Si as a function of temperature. The Fermi level, E_F , in the phosphorus (10^{20} cm^{-3}) in-diffused region is indicated by the solid black line. The E_F curves for phosphorus-doped and boron-doped wafers with resistivities of 0.5, 1.0, and 5.0 Ωcm approach and then equal the intrinsic Fermi level, E_i , above 500 °C. E_F -dependent physical phenomena driving the redistribution of Fe during PDG are thus similar in n -type and p -type mc-Si during PDG.

intrinsic Fermi level. This has important implications for transition-metal diffusion and segregation. The physics underlying PDG are the nucleation and subsequent growth or dissolution of precipitates, the solid solubility, and the diffusivity of metal point defects.²⁴ This study provides evidence that the trends in these physical driving forces are similar in *n*- and *p*-type silicon at PDG process temperature for deep level defects. The nucleation and subsequent growth or dissolution of precipitates do not depend on the base doping type when nucleation occurs at high temperature,²⁵ but rather on the local temperature-dependent solid solubility, the local dissolved species concentration, the precipitate size, the surface energy, lattice strain, and the morphology of the precipitate.^{26–30} The solid solubility of doped Si is enhanced compared to that of intrinsic Si, but the enhancement is similar for Fermi levels that are equidistant from midgap.^{23,31,32} Finally, the diffusivity of metals in Si depends on the relative concentrations of charged and neutral species. For a wide range of parameters, including doping type and varying relative concentrations of charged and neutral Fe, the diffusivity of Fe in Si can be relatively well described with a single straight line fit.²³ At higher temperatures, the majority of the Fe is neutral because the Fermi level is at or close to the midgap as discussed above.²³

Modeling indicates that the $>500 \mu\text{s}$ lifetimes measured after PDG in this 6N's UMG *n*-type mc-Si are long enough to support high-efficiency solar cells.^{6,33} The lifetime trends are also similar to those in a similar study of *p*-type mc-Si that was gettered at 820 °C, 870 °C, and 920 °C.¹⁰ For both materials, the average lifetimes increased by over an order of magnitude, and the lifetime was longest after PDG at the intermediate temperature.

Our results are consistent with the hypothesis that, as with *p*-type mc-Si,^{24,34} removal of both precipitated and point defect impurities is likely important for maximizing lifetime in *n*-type mc-Si. Further comparative investigation, including the effect of hydrogen passivation³⁵ on defect recombination activity, measurements of the recombination activity of individual metal-rich precipitates, and further perturbations of the time-temperature profile parameters, is needed to clarify the role of the metal impurity distribution in the performance of *n*-type mc-Si and thus how to process it to extract its full performance potential.

In summary, using a combination of synchrotron-based μ -XRF mapping of >250 metal-rich particles and PC-PL lifetime imaging, we show that metal impurities in industrially grown *n*-type UMG mc-Si are getterable and that PDG improves minority carrier lifetime by over an order of magnitude. PDG at temperatures as low as 820 °C fully removed Cu-, Ni-, and Co-rich particles to below detection limits. We achieved partial removal of Fe with PDG at 880 °C and a 920 °C process removed all precipitated transition metals to below detection limits. PDG at 820 °C for 30 min and 60 min resulted in similar precipitated Fe distributions, indicating that precipitate dissolution may saturate after 30 min or less, pointing to an opportunity to shorten processing without sacrificing precipitate remediation. Our results are consistent with calculations showing that the physical mechanisms underlying the redistribution of metals during PDG are similar for *n*-type and *p*-type mc-Si.

We thank S. Meyer, S. Wahl, S. Ramanathan, S. A. McHugo, and H. S. Laine. Funding provided by the National Science Foundation (NSF) and the Department of Energy (DOE) under NSF CA No. EEC-1041895. μ -XRF was performed at the Advanced Photon Source, a U.S. DOE Office of Science User Facility operated for the DOE Office of Science by Argonne National Laboratory under Contract No. DE-AC02-06CH11357. EBSD and ALD performed at the Center for Nanoscale Systems (CNS), a member of the National Nanotechnology Infrastructure Network, which is supported by NSF Award No. ECS-0335765. CNS is part of Harvard University. A.E.M. acknowledges the Department of Defense through the NDSEG fellowship program. M.A.J. and P.X.T.Y. acknowledge support by the NSF Graduate Research Fellowship under Grant No. 1122374. D.P.F. acknowledges support by the Martin Family Society of Fellows for Sustainability and the University of California, San Diego.

¹D. Macdonald and L. J. Geerligs, "Recombination activity of interstitial iron and other transition metal point defects in *p*- and *n*-type crystalline silicon," *Appl. Phys. Lett.* **85**, 4061 (2004).

²G. Coletti, R. Kvande, V. D. Mihailetschi, L. J. Geerligs, L. Arnberg, and E. J. Øvrelid, "Effect of iron in silicon feedstock on *p*- and *n*-type multicrystalline silicon solar cells," *J. Appl. Phys.* **104**, 104913 (2008).

³J. Schmidt, B. Lim, D. Walter, K. Bothe, S. Gatz, T. Dullweber, and P. P. Altermatt, "Impurity-related limitations of next-generation industrial silicon solar cells," *IEEE J. Photovoltaics* **3**, 114–118 (2013).

⁴A. Cuevas, S. Riepe, M. J. Kerr, D. H. Macdonald, G. Coletti, and F. Ferrazza, "N-type multicrystalline silicon: A stable, high lifetime material," in *Proceedings of 3rd World Conference on Photovoltaic Energy Conversion, 2003* (IEEE, 2003), pp. 1312–1315, Vol. 2.

⁵V. Vähänissi, M. Yli-Koski, A. Haarahluntunen, H. Talvitie, Y. Bao, and H. Savin, "Solar energy materials & solar cells," *Sol. Energy Mater. Sol. Cells* **114**, 54–58 (2013).

⁶F. Schindler, B. Michl, A. Kleiber, H. Steinkemper, J. Schön, W. Kwapil, P. Krenckel, S. Riepe, W. Warta, and M. C. Schubert, "Potential gain in multicrystalline silicon solar cell efficiency by *n*-type doping," *IEEE J. Photovoltaics* **5**, 499–506 (2015).

⁷J. Schön, F. Schindler, W. Kwapil, and M. Knörlein, "Identification of the most relevant metal impurities in mc *n*-type silicon for solar cells," *Sol. Energy Mater. Sol. Cells* **142**, 107–115 (2015).

⁸F. Schindler, B. Michl, P. Krenckel, S. Riepe, and F. Feldmann, "Efficiency potential of *p*- and *n*-type high performance multicrystalline silicon," *Energy Proc.* **77**, 633–638 (2015).

⁹J. Hofstetter, D. P. Fenning, D. M. Powell, A. E. Morishige, H. Wagner, and T. Buonassisi, "Sorting metrics for customized phosphorus diffusion gettering," *IEEE J. Photovoltaics* **4**, 1421–1428 (2014).

¹⁰D. P. Fenning, A. S. Zuschlag, M. I. Bertoni, B. Lai, G. Hahn, and T. Buonassisi, "Improved iron gettering of contaminated multicrystalline silicon by high-temperature phosphorus diffusion," *J. Appl. Phys.* **113**, 214504 (2013).

¹¹B. Michl, J. Schön, W. Warta, and M. C. Schubert, "The impact of different diffusion temperature profiles on iron concentrations and carrier lifetimes in multicrystalline silicon wafers," *IEEE J. Photovoltaics* **3**, 635–640 (2013).

¹²J. Schön, H. Habenicht, M. C. Schubert, and W. Warta, "Understanding the distribution of iron in multicrystalline silicon after emitter formation: Theoretical model and experiments," *J. Appl. Phys.* **109**, 063717 (2011).

¹³W. Kwapil, J. Schön, F. Schindler, W. Warta, and M. C. Schubert, "Impact of iron precipitates on carrier lifetime in as-grown and phosphorus-gettered multicrystalline silicon wafers in model and experiment," *IEEE J. Photovoltaics* **4**, 791–798 (2014).

¹⁴See supplementary material at <http://dx.doi.org/10.1063/1.4950765> for further detailed experimental results.

¹⁵M. A. Jensen, J. Hofstetter, A. E. Morishige, G. Coletti, B. Lai, D. P. Fenning, and T. Buonassisi, "Synchrotron-based analysis of chromium distributions in multicrystalline silicon for solar cells," *Appl. Phys. Lett.* **106**, 202104 (2015).

¹⁶T. Buonassisi, M. Heuer, O. F. Vyvenko, A. A. Istratov, E. R. Weber, Z. Cai, B. Lai, T. F. Ciszek, and R. Schindler, "Applications of synchrotron radiation X-ray techniques on the analysis of the behavior of transition

- metals in solar cells and single-crystalline silicon with extended defects,” *Phys. B: Condens. Matter* **340–342**, 1137–1141 (2003).
- ¹⁷Y. Dusausoy, J. Protas, R. Wandji, and B. Roques, “Structure Cristalline du Disiliciure de fer, $\text{FeSi}_2\beta$,” *Acta Crystallogr., Sect. B: Struct. Crystallogr. Cryst. Chem.* **27**, 1209 (1971).
- ¹⁸D. P. Fenning, J. Hofstetter, M. I. Bertoni, G. Coletti, B. Lai, C. del Cañizo, and T. Buonassisi, “Precipitated iron: A limit on gettering efficacy in multicrystalline silicon,” *J. Appl. Phys.* **113**, 044521 (2013).
- ¹⁹J. Hofstetter, D. P. Fenning, M. I. Bertoni, J. F. Lelièvre, C. del Cañizo, and T. Buonassisi, “Impurity-to-efficiency simulator: Predictive simulation of silicon solar cell performance based on iron content and distribution,” *Prog. Photovoltaics* **19**, 487–497 (2011).
- ²⁰S. Herlufsen, J. Schmidt, D. Hinken, K. Bothe, and R. Brendel, “Photoconductance-calibrated photoluminescence lifetime imaging of crystalline silicon,” *Phys. Status Solidi RRL* **2**, 245–247 (2008).
- ²¹A. Thompson, D. Attwood, E. Gullikson, M. Howells, K.-J. Kim, J. Kirz, J. Kortright, I. Lindau, Y. Liu, P. Pianetta, A. Robinson, J. Scofield, J. Underwood, G. Williams, and H. Winick, *X-Ray Data Booklet* (Lawrence Berkeley National Laboratory, 2009), pp. 1–176.
- ²²E. R. Weber, “Transition metals in silicon,” *Appl. Phys. A: Mater. Sci. Process.* **30**, 1–22 (1983).
- ²³A. A. Istratov, H. Hieslmair, and E. R. Weber, “Iron and its complexes in silicon,” *Appl. Phys. A: Mater. Sci. Process.* **69**, 13–44 (1999).
- ²⁴A. E. Morishige, H. S. Laine, J. Schön, A. Haarahiltunen, J. Hofstetter, C. del Cañizo, M. C. Schubert, H. Savin, and T. Buonassisi, “Building intuition of iron evolution during solar cell processing through analysis of different process models,” *Appl. Phys. A: Mater. Sci. Process.* **120**, 1357–1373 (2015).
- ²⁵H.-W. Guo and S. T. Dunham, “Accurate modeling of copper precipitation kinetics including Fermi level dependence,” *Appl. Phys. Lett.* **89**, 182106 (2006).
- ²⁶A. Haarahiltunen, H. Väinölä, O. Anttila, E. Saarnilehto, M. Yli-Koski, J. Storgårds, and J. Sinkkonen, “Modeling of heterogeneous precipitation of iron in silicon,” *Appl. Phys. Lett.* **87**, 151908 (2005).
- ²⁷S. T. Dunham, “Growth kinetics of disk-shaped extended defects with constant thickness,” *Appl. Phys. Lett.* **63**, 464 (1993).
- ²⁸H. Takahashi and H. Yamada-Kaneta, “Iron gettering controlled by size and density of oxygen precipitates in Czochralski-grown silicon,” *Jpn. J. Appl. Phys., Part 1* **37**, 1689 (1998).
- ²⁹S. A. McHugo, E. R. Weber, M. Mizuno, and F. G. Kirscht, “A study of gettering efficiency and stability in Czochralski silicon,” *Appl. Phys. Lett.* **66**, 2840 (1995).
- ³⁰A. Mesli, T. Heiser, N. Amroun, and P. Siffert, “Charge-state-dependent iron precipitation in silicon,” *Appl. Phys. Lett.* **57**, 1898 (1990).
- ³¹D. Gilles, W. Schröter, and W. Bergholz, “Impact of the electronic-structure on the solubility and diffusion of 3d transition-elements in silicon,” *Phys. Rev. B* **41**, 5770–5782 (1990).
- ³²S. A. McHugo, R. J. McDonald, A. R. Smith, D. L. Hurley, and E. R. Weber, “Iron solubility in highly boron-doped silicon,” *Appl. Phys. Lett.* **73**, 1424 (1998).
- ³³J. Hofstetter, C. del Cañizo, H. Wagner, S. Castellanos, and T. Buonassisi, “Material requirements for the adoption of unconventional silicon crystal and wafer growth techniques for high-efficiency solar cells,” *Prog. Photovoltaics* **24**, 122–132 (2016).
- ³⁴D. P. Fenning, J. Hofstetter, A. E. Morishige, D. M. Powell, A. Zuschlag, G. Hahn, and T. Buonassisi, “Darwin at high temperature: Advancing solar cell material design using defect kinetics simulations and evolutionary optimization,” *Adv. Energy Mater.* **4**, 1400459 (2014).
- ³⁵C. Sun, F. E. Rougieux, and D. Macdonald, “A unified approach to modelling the charge state of monatomic hydrogen and other defects in crystalline silicon,” *J. Appl. Phys.* **117**, 045702 (2015).